Aerodynamic Study of Two Opposing Moving Trains in a Tunnel Based on Different Nose Contours

W. H. Li[†], T. H. Liu, J. Zhang, Z. W. Chen, X. D. Chen and T. Z. Xie

Key Laboratory of Traffic Safety on Track, Ministry of Education, School of Traffic and Transportation Engineering, Central South University, Changsha 410075, Hunan, China

†*Corresponding Author Email:lwh@csu.edu.cn*

ABSTRACT

It is well known that the train nose shape has significant influence on the aerodynamic characteristics. This study explores the influence of four kinds of nose shapes (fusiform, flat-broad, bulge-broad, ellipsoidal) on the aerodynamic performance of two opposing high-speed trains passing by each other through a tunnel at 250 km/h. The method of three dimensional, compressible, unsteady Reynolds-averaged Navier-Stokes equations and RNG k-ε double equation turbulence model was carried out to simulate the whole process of two trains passing by each other inside a tunnel. Then the pressure variations on tunnel wall and train surface are compared with previous full-scale test to validate the numerical method adopted in this paper. The assessment characteristics, such as transient pressure and aerodynamic loading, are analyzed to investigate the influence of nose shape on these assessment parameters. It is revealed that aerodynamic performance of trains which have longitudinal nose profile line B (fusiform, flat-broad shape) is relatively better when passing by each other in a tunnel. The results can be used as a guideline for high-speed train nose shape design.

Keywords: High-speed train (HST); Nose shape; Railway tunnel; Transient pressure; Aerodynamic loading.

NOMENCLATURE

EX	Tunnel Exit	u	mean velocity
EN	Tunnel Entrance		
k	kinetic energy of turbulence	μ	dynamic viscosity of the air
NN	Nose and Nose	μ_t	turbulent viscosity
NT	Nose and Tail	μ_{eff}	sum of kinetic and turbulent viscosities
MPW	Micro Pressure Wave	ρ	air density
p	mean pressure	ε	turbulent dissipation rate
TT	Tail and Tail		

1. INTRODUCTION

In recent years, with the increase of railway vehicle speed, a series of aerodynamic issues are provoked by a high-speed train suddenly enters into a tunnel, including transient pressure both on train surface and tunnel wall (Kwon *et al.* 2003; Riccoa *et al.* 2007), micro pressure wave (MPW) at tunnel portal (Ozawa *et al.*1988), slipstream in tunnel *et al.* (Gilbert *et al.* 2013, Yang *et al.* 2013). These effects would lead to passenger discomfort, environmental noise and potential damage to the tunnel facilities and vehicle body (Wittkowski *et al.* 2015). Hwang *et al.* (2013) reported that when two opposing moving trains passing by each other in a tunnel in

particular, the pressure variation and aerodynamic loading acting on train body would be much stronger and the flow phenomenon is more complicated than that of a single train passing through a tunnel. Studies to solve the aerodynamic problems related to two trains meeting in a tunnel were performed lately. Chu *et al.* (2014) carried out several numerical calculations to explore the influence of the vehicle speed, the blockage ratio, the tunnel length and the intersecting location on the tunnel pressure waves generated by the trains. Zhang *et al.* (2011) conducted a numerical study to solve the flow around two high speed trains passing by each other at the same speed in a long tunnel. Fujii *et al.* (1995) revealed that when two opposing
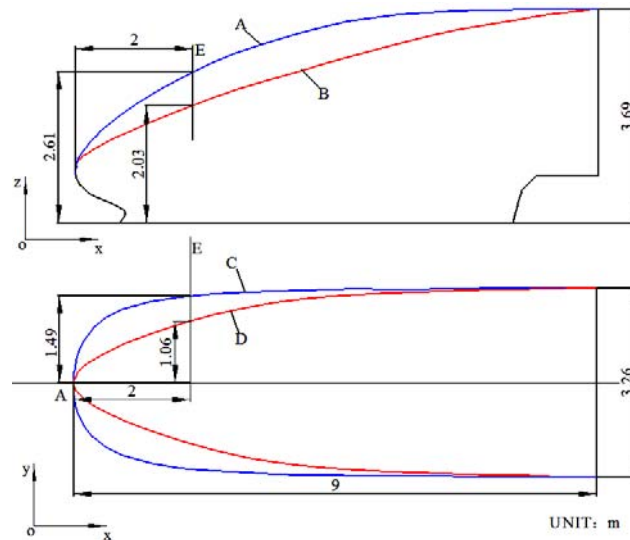
Fig. 1. Different longitudinal and horizontal nose profiles of high-speed train.

trains encounter each other in a tunnel, the trains are firstly pushed laterally away from each other due to the high pressure region on train nose, but the side force changes the direction and pushes the trains towards each other when they are paralleled side by side. In addition, it was revealed that the lift force was insignificant and can be neglected in this issue compared to the drag and side force.

It is acknowledged that the tunnel cross-sectional area should be enlarged or the cross-sectional area of the train body should be diminished to lower the aerodynamic effects (Xiang *et al.* 2010, Ku *et al.* 2010). For this purpose, the cross-sectional area of present high-speed train gets smaller while the tunnel becomes larger than before. However, it seems impossible for the cross-sectional area of the train gets smaller than a certain design limit, and the tunnel cross-section cannot be expanded further due to the tremendous construction costs. But according to previous studies, train aerodynamic performance is also influenced by the nose shape. Based on three-dimensional numerical simulation, Choi *et al.* (2014) evaluated the aerodynamic effects based on the different the train nose lengths and the tunnel cross-sectional areas, it was revealed that the aerodynamic drag in a tunnel can be minimized up to around 50% by changing the train nose type from a blunt to a streamlined shape. Munoz-Paniagua *et al.* (2015) performed an optimization study of the nose shape of a high-speed train in the open air using the adjoint method, the method was demonstrated to be effective and a significant reduction of the aerodynamic drag was aimed. By adopting a newly introduced regression technique, Lee *et al.* (2007) conducted a study on the nose shape design of high-speed trains to reduce the peak value of micro pressure wave (MPW), the design results showed that appropriate optimization on nose shape can lower the strength of MPW.

In view of the above studies, there is a need to assess the aerodynamic performance of trains with different nose shapes passing by each other in a

tunnel. Some of the previous studies paid attention on the aerodynamic influence of train nose shape in the open air or on a single train running through a tunnel. Others focused on the factors such as the tunnel length, tunnel hood, the blockage ratio, the train speed and other parameters on the aerodynamics when two opposing moving trains meeting each other inside a tunnel. However, the influence of train nose shape on the aerodynamics of two opposing moving trains meeting in a tunnel was not considered. Therefore, the aim of this work is to utilize a three-dimensional, compressible, turbulence model to investigate the aerodynamic performance of high-speed trains with different nose shapes passing by each other through a tunnel. Assessment is performed by analyzing their aerodynamic loading and transient pressure on train surface and tunnel wall. The results can provide certain guidance for the high-speed train nose shape design.

2. SCENARIO OF NOSE SHAPE FOR HIGH-SPEED TRAIN

The nose shape of high-speed train has certain influence on its lateral force, lift, drag and wake (Ikeda *et al.* 2003). Generally, within constrained design space, the longer streamline length of a train, the better aerodynamic performance it has. However, too longer streamline length may lead to reduction of passenger capacity, thus decreasing railway operation efficiency. Therefore we should primarily choose the appropriate streamline length according to the design speed and running condition. Then some proper adjustment on the horizontal and longitudinal train nose profile lines can be added to improve the aerodynamic performance further. Based on different nose contours, this paper designed four nose shapes by combining two kinds of longitudinal profile lines (A, B) and two kinds of horizontal profile lines (C, D) as presented in Fig. 1. Fig. 2 shows these four
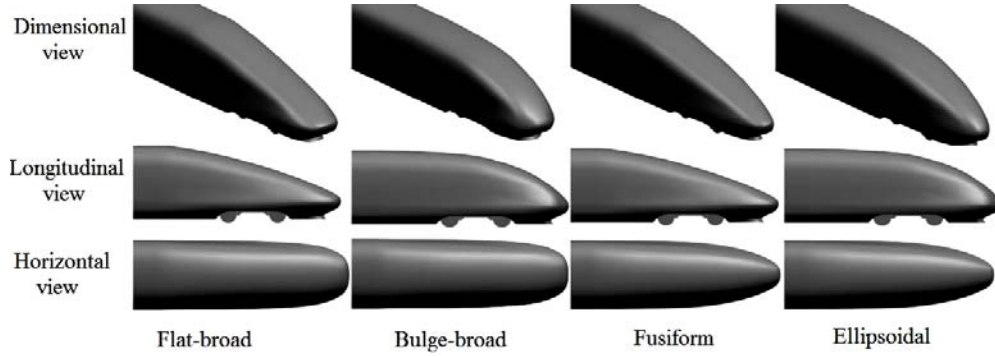
Fig. 2. Views of trains with different nose shapes from different directions.

nose shapes: bulged-broad (A+C), ellipsoidal (A+D), flat-broad (B+C), fusiform (B+D). Note that the bulged-broad and ellipsoidal shapes both have the same longitudinal nose profile line A while the flat-broad and fusiform shapes both have the same longitudinal nose profile line B. Similarly, the horizontal nose profile line C is applied both for the bulged-broad and flat-broad shapes while the horizontal nose profile line D is both applied for fusiform and ellipsoidal shapes. The other parameters such as streamline length (9 m), total train length (201.6 m) all remain the same. In order to accurately simulate the case of train/train intersection in a tunnel, the train model adopts 8-car unit, namely the head car, six middle cars and the tail car, including the bogies and windshields, which is the same as actual conditions. Meanwhile, small objects with complex structures like roof pantographs, lights and handlebars have been omitted to save computing resources.

3. NUMERICAL SIMULATION MODEL

3.1 Mathematical Model

In this work, the train speed is 250 km/h and the length of the tunnel is 1000 m. Although the train speed is less than Mach number 0.3, the space inside the tunnel is confined by the tunnel wall and train body, so the air is supposed to be compressible, namely ideal gas. To understand the aerodynamic phenomenon caused by two opposing trains passing by each other through a tunnel, an unsteady, compressible, renormalization group (RNG) k-ε turbulence model was applied. The RNG k-ε turbulence model has been recently proved to be effective to simulate the aerodynamic effects generated by train/tunnel entry or train/train passing by each other in a tunnel (Chu *et al.* 2014; Li *et al.* 2016; Niu *et al.* 2017), so it was also adopted in this work.

The governing equations of the continuity equation and RANS equations are listed as follows:

$$\frac{\partial \rho}{\partial t} + \frac{\partial}{\partial x_i}\left(\rho u_i\right) = 0 \tag{1}$$

$$\frac{\partial(\rho u_i)}{\partial t} + \frac{\partial}{\partial x_j}\left(\rho u_i u_j\right) = -\frac{\partial p}{\partial x_i} +$$
$$\frac{\partial}{\partial x_j}\left[\mu\left(\frac{\partial u_i}{\partial x_j} + \frac{\partial u_j}{\partial x_i} - \frac{2}{3}\delta_{ij}\frac{\partial u_l}{\partial x_l}\right)\right] \tag{2}$$
$$+ \frac{\partial}{\partial x_j}\left(-\overline{\rho u_i' u_j'}\right) + \rho g\delta_{i3}$$

where ρ is the air density, p and u are the mean pressure and velocity, μ is the dynamic viscosity of the air, the subscripts $i,j,l = 1, 2, 3$, represent the x, y, and z directions respectively.

The time-averaged Reynolds stress $\overline{\rho u_i' u_j'}$ can be expressed as the mean velocity gradients via the Boussinseq hypothesis:

$$-\overline{\rho u_i' u_j'} = \mu_t\left(\frac{\partial u_i}{\partial x_j} + \frac{\partial u_i}{\partial x_j}\right)$$
$$-\frac{2}{3}\left(\rho k + \mu_t\frac{\partial u_k}{\partial x_k}\right)\delta_{ij} \tag{3}$$

$$\mu_t = \rho C_\mu \frac{k^2}{\varepsilon} \tag{4}$$

here μ_t is the turbulent viscosity and k is the turbulent kinetic energy, the model coefficient $C_\mu = 0.0845$. To make the above equations closed, the turbulent kinetic energy and the energy dissipation rate equations are presented as follow:

$$\frac{\partial(\rho k)}{\partial t} + \frac{\partial}{\partial x_i}\left(\rho k u_i\right) =$$
$$\frac{\partial}{\partial x_j}\left[\alpha_k \mu_{eff}\frac{\partial k}{\partial x_j}\right] + G_k + \rho\varepsilon \tag{5}$$

$$\frac{\partial(\rho\varepsilon)}{\partial t} + \frac{\partial(\rho\varepsilon u_i)}{\partial x_i} =$$
$$\frac{\partial}{\partial x_j}\left[\alpha_\varepsilon \mu_{eff}\frac{\partial\varepsilon}{\partial x_j}\right] + \frac{C_{1\varepsilon}^*}{k}G_k - C_{2\varepsilon}\rho\frac{\varepsilon^2}{k} \tag{6}$$

where μ_{eff} is the sum of kinetic and turbulent viscosities. α_ε and α_k are the reciprocal of the
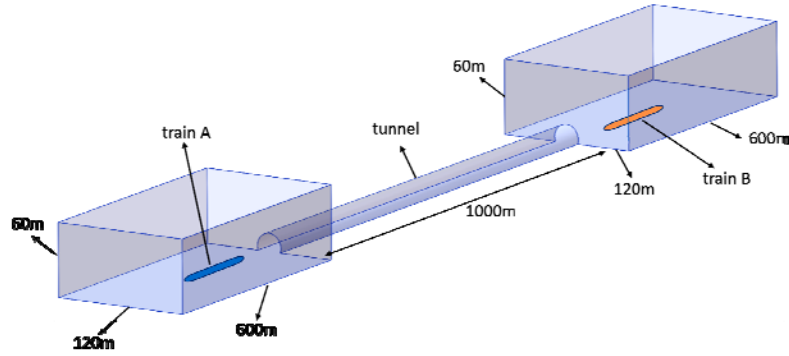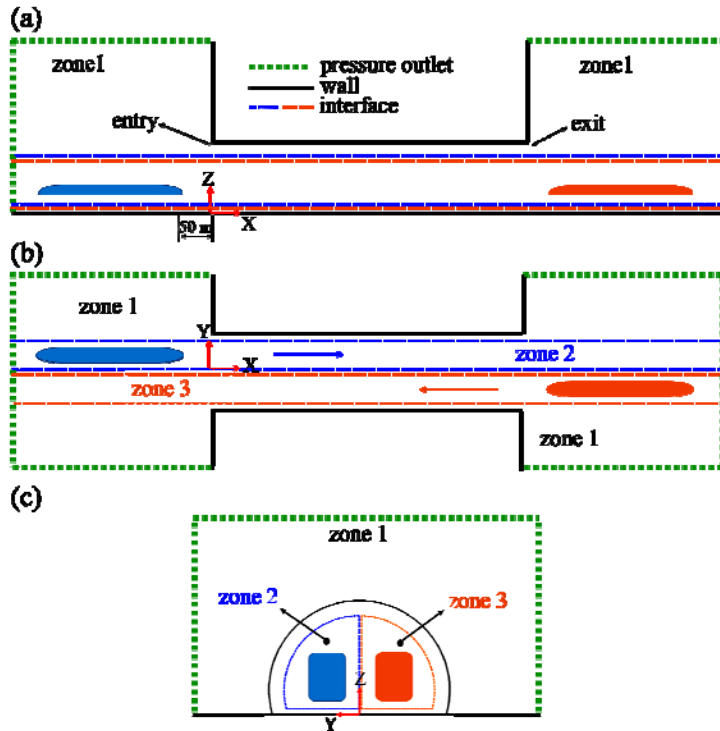
Fig. 3. Computational domain.

Fig. 4. Schematic diagram of the computation domain and boundary conditions: (a) side view; (b) top view; (c) cross-sectional view.

turbulent kinetic energy and the dissipation rate, respectively. G_k is the generated item of turbulent kinetic energy caused by the mean velocity gradient. The model coefficients $C_{1\varepsilon}^*$ and $C_{2\varepsilon}$ are given by:

$$C_{1\varepsilon}^* = C_{1\varepsilon} - \frac{\eta\left(1 - \eta / \eta_0\right)}{1 + \beta\eta^3} \tag{7}$$

$$\eta = \left(2E_{ij} \cdot 2E_{ij}\right)^{1/2} \frac{k}{\varepsilon} \tag{8}$$

$$E_{ij} = \frac{1}{2}\left(\frac{\partial u_i}{\partial x_j} + \frac{\partial u_j}{\partial x_i}\right) \tag{9}$$

where $C_{1\varepsilon}$=1.42, $C_{2\varepsilon}$=1.68, η_0=4.377, β=0.012.

The governing equations above were solved by commercial software Fluent 6.3.26 and the computation domain was discretized by the Finite Volume Method (FVM). Additionally, the standard wall function is applied to handle the airflow near wall region.

3.2 Computational Domain and Boundary Conditions

The computational domain of the simulation is demonstrated in Fig. 3 and Fig. 4. The whole computational domain consists of the stationary region of zone 1 and the sliding regions of zone 2 and zone 3. Zone 2 and zone 3 contains train A and train B respectively while zone 1 contains the tunnel domain and the outer domain. The outer domain is simulated as two rectangular bodies

1378

which are 600 m in length, 120 m in width and 60 m in height as demonstrated in Fig 4. The dimensions are chosen to guarantee the flow near the tunnel entrance is not affected by outer domain. To realize the relative motion and data exchange between the trains and the surroundings, sliding mesh method was utilized between zone 1/zone 2, zone 1/zone 3 and zone 2/zone 3 through pairs of grid interfaces as illustrated in Fig. 4. Unlike dynamic mesh technique which need mesh regeneration to realize the relative movement, by using sliding mesh method, train domains of zone 1 and zone 2 can slide relatively by each another along *x*-axis without mesh regeneration. The tunnel chosen in this work is a double-track tunnel whose cross-sectional area is 80 m², and the blockage ratio, which is the sectional area of carriage divided by the tunnel sectional area, is 14.04%. The tunnel is 1000 m in length and the distance between the centers of tracks is 4.4 m. The train is placed in the left side of the tracks along the tunnel due to the regulation that the trains of the railway in China are left-sided.

The motion of the train is defined via the user-defined function (UDF), which is 69.44 m/s and -69.44 m/s for train A and train B respectively. The fixed region of the tunnel and ground are treated as hexahedral grid. Because of the complex shape of the train body, sliding region of the train domains (zone 2 and zone 3) are discretized by more adaptive non-structured grid. Small size grid is utilized close to the train body so as to simulate the boundary layer, the thickness of the first layer is 1.5 mm and the y+ around the train surface is nearly 240, which basically meets the demands of the RANS model. The surface grid of the train body and tunnel portal are illustrated in Fig. 5. The total number of the grid elements is about 3.0×10^7. The time step for unsteady computing is 6×10^{-3}s, which is sufficient to solve the unsteady flow field in the tunnel. Commercial software FLUENT is used to simulate the whole train movement in the tunnel.

Because the train starts in the open field, the pressure outlet boundary condition is added to the outer domain. As presented in Fig. 4, no-slip wall boundary conditions are utilized for the train body, the tunnel wall and the ground. To ensure the stability of the flow filed when the trains suddenly enter into the tunnel, the two trains are both placed in 50 m from the tunnel portals.

3.3 Measuring Points Layout

Due to the symmetrical case when two opposing moving trains passing by each other through a tunnel, the measuring points are set only on one train's surface. The main purpose of this paper is focusing on the aerodynamic performance influenced by different train nose shapes. Therefore, more measuring points are set on the head and tail car. As demonstrated in Fig. 6, the head car has 7 measuring points on the train surface, and each middle car has 2 measuring points at the symmetrical locations. Measuring point layout on the tail car is the same as the head car, the serial number is identified from head to tail successively.

Thus the amount of measuring points is 26 in total (2×7+6×2=26). The serial numbers in the bracket represent the measuring points on the other side of train surface, which is the intersection side as illustrated in Fig. 7(a). Apparently, the serial numbers outside the bracket represent the measuring points of the non-intersection side. To investigate the pressure transient inside the tunnel, 9 measurement points are set on the tunnel wall at the height of 4.2 m from the ground, which is shown in Fig. 7(b).
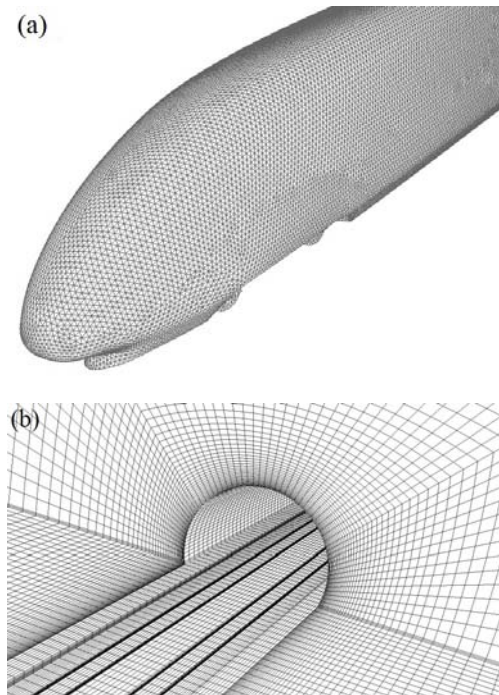

Fig. 5. Grid of train surface and tunnel zone: (a) train surface; (b) tunnel portal.

4. MODEL VALIDATION

In 2008, series of full-scale tests at 200-250 km/h on tunnel aerodynamics were carried out in Hefei-Wuhan high-speed railway in China. To verify the calculation algorithm adopted in the paper, the present model was applied to simulate the full scale test through Yingzuishi tunnel at the target speed of 213 km/h. The parameters of the trains and the tunnel in the numerical simulation were the same as the full-scale test. The train used in the test was CRH2A (Fig. 8b), whose length was 201.4 m. The tunnel cross-sectional area was 92 m² with a length of 1080 m. Pressure transducers produced by Kulite Semiconductor Products Corporation in America were used to monitor the pressure variation on the train surface, and the range of the transducer was 15 psi. The location of two trains passing by each other was at 344 m from the tunnel entrance. The portal of Yingzuishi tunnel and the test train were shown in Fig. 8.

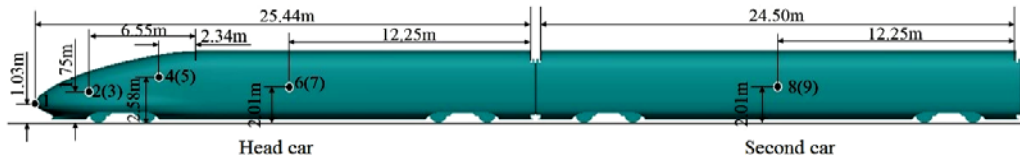Two points were used to compare the pressure waves obtained from the full-scale test and the

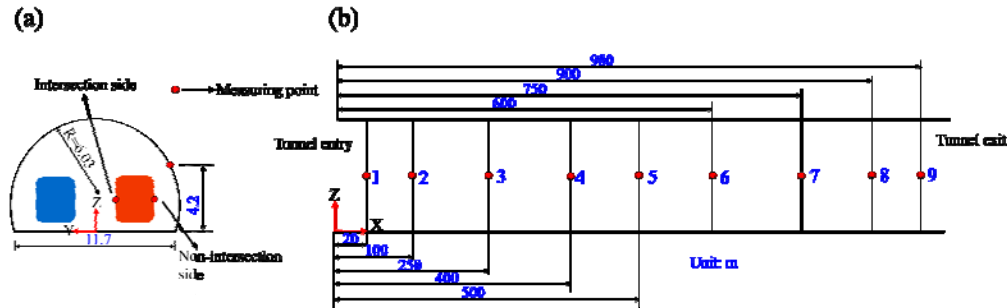**Fig. 6. Measuring point layout on train surface.**

Fig. 7. Measuring point layout on tunnel wall: (a) cross-sectional view; (b) longitudinal view.
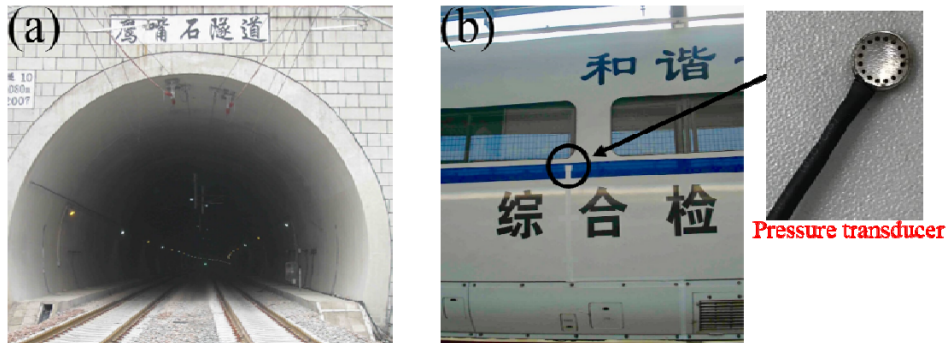

Fig. 8. Tunnel and the train used in the full-scale test: (a) portal of Yingzuishi tunnel; (b) second car of the CRH2A train with sensors.
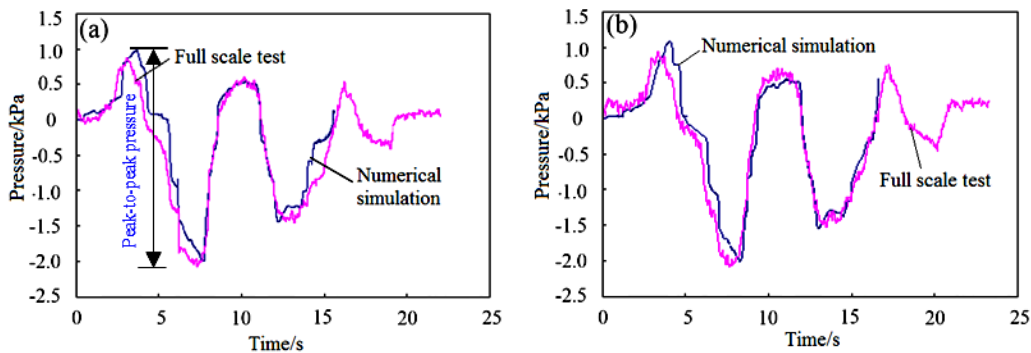

Fig. 9. Comparisons between the calculated and experimental results of the time-pressure history on train surface: (a) No. 6 measuring point on the head car; (b) No. 8 measuring point on the second car.

numerical simulation: one point was on the middle of the head car (No. 6 point, refer to Fig. 6), and the other is on the middle of the second car (No. 8 point). As indicated in Fig. 9, the pressure waveforms between the simulation and the experiment showed good agreement with each other. The peak-to-peak pressure value, which is the

difference between the positive maximum pressure and the negative maximum pressure, is used to estimate the pressure variation inside the tunnel. In Fig. 8(a) the peak-to-peak pressure value of No. 6 point obtained from simulation and field test was 3098 Pa and 2956 Pa respectively, the error of which is 4.8%. In Fig. 9(b) the peak-to-peak

Table 1 Peak-to-peak pressure value on tunnel wall

Distance from tunnel entrance /m	Peak-to-peak pressure value / Pa				
	Bulge-broad	Ellipsoidal	Flat-broad	Fusiform	Maximum deviation
20	2578	2546	2462	2465	4.7%
100	3211	3176	3108	3114	3.3%
250	6180	6152	6118	6144	1.0%
400	6575	6523	6484	6492	1.4%
500	6040	5946	5862	5847	3.3%
600	6642	6564	6518	6537	1.9%
750	6134	6094	6084	6089	0.8%
900	3115	3083	3015	3007	3.6%
980	2531	2512	2475	2477	2.2%

pressure value of No. 8 point for simulation and field test was 2963 Pa and 2896 Pa respectively, with an error of 2.3%. The largest pressure differences were both less than 5%. Therefore the numerical simulation method adopted in this paper was relatively accurate to reflect the aerodynamic effects caused by two opposing trains passing by each other through a tunnel. Additionally, from the comparisons of these two measuring points, it was found that the numerical results were slightly larger than that of the experimental data. The main reason was assumed that the train speed inside the tunnel during the test was slightly lower than the target speed due to the actual conditions.

5. RESULTS AND DISCUSSION

5.1 Pressure Transient on Tunnel Wall

Table 1 presents the peak-to-peak pressure values at different longitudinal locations on tunnel wall. As can be seen from the table, due to the propagation of pressure waves inside the tunnel, the pressure at different longitudinal locations on tunnel wall at the same height varies different, however the influencing rules of the pressure generated by trains of the four different nose shapes are almost identical. The pressure variation at the tunnel portals is relatively low. The largest pressure variations all occur on the tunnel wall 600 m from the entrance. At the symmetrical locations on the tunnel wall in longitudinal direction, say at 20 m and 980 m from the tunnel entrance, the pressure variations are nearly identical because of the symmetrical movements of the two opposing trains. With the increase of the distance from tunnel entrance, the pressure values rise firstly (entrance to 2/5 of the tunnel length), afterwards decline and then rise again (2/5 to 3/5 of the tunnel length), finally decline all the way (3/5 of the tunnel length to exit). Fig. 10 demonstrates the pressure variations of three

typical locations inside the tunnel. The pressure variation at x=20 m near the tunnel portal is lower because the train does not fully enter into the tunnel, and the compression wave has not fully developed yet. The pressure variation becomes more significant further inside the tunnel such as x=400m and x=500 m due to the nose-entry compression which fully has been developed. Generally, the pressure variations in the tunnel are very complex due to the superposition of reflected waves and passing-by of the trains, the positive maximum pressure measured on the tunnel wall is induced by the nose-entry compression wave while the negative maximum pressure is not only affected by the expansion wave but also influenced by the passing-by of the trains (Ko *et al.* 2012). When the train passes through a certain location inside the tunnel, the surrounding air will be driven to move accordingly, the pressure waveforms of x=400 m and x=500 m in Fig.10 have a sudden drop at t=6.5 and t=7.9 s respectively due to the nose passing-by of train A. When the nose passing-by encounters the expansion wave of x=400 m at t=6.5 s, the negative maximum pressure will be reinforced, however, when the nose passing-by encounters the compressive wave of x=500 m at t=7.9 s, the negative maximum pressure will be reduced accordingly. Whereas the nose-entry induced maximum positive pressure of these two points are approximately identical. As a result, the peak-to-peak pressure at x=500 is lower than that at x=400 m. Among the four nose shapes, the largest pressure variation is induced by bulge-broad shape at x=600 m, and the largest deviation reaches 4.7% at x=20 m among the four shapes. Notice that the pressure variations between bulged-broad and ellipsoidal shape, as well as flat-broad and fusiform shape are closer to each other while between these two groups there is relatively a larger gap. This is mainly because the two groups both have same longitudinal nose profile lines.
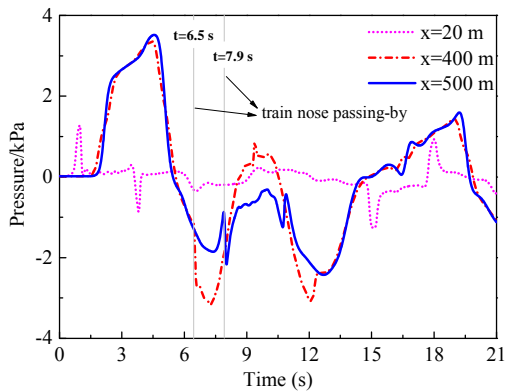
Fig. 10. Time-pressure histories of three typical points on the tunnel wall of ellipsoidal shape.

When a high-speed train suddenly moves into a tunnel, a compression wave is induced and travels through the tunnel at sonic speed, once the compression wave arrives at the tunnel portal, part of the wave is reflected backwards and part is emitted outside the tunnel which leads to booming noise and vibration. Such phenomenon is the so-called micro pressure wave (MPW). The strength of the MPW is largely determined by the peak pressure gradient of the initial compression wave (Kikuchi *et al.* 2011). Therefore, it is possible to reduce the MPW by diminish the pressure gradient of the initial compression wave. It is maybe one of the most available methods to reduce MPW with relatively lower cost by optimizing the nose shape of the train. The initial compression waves of measuring point No. 1 at *x*=20 m and No. 5 at *x*=500 m are shown in Fig. 11. As can be seen, the waveforms of these two measuring points are different due to their different locations along the tunnel. The difference of the waveforms among the four nose shapes is more obvious near the tunnel portal but differs slightly further inside the tunnel. The pressure rise of No. 1 point near the tunnel portal is mainly induced by the train nose-entry, hence, the influence of the train nose shape is dominant. The No. 5 measuring point, however, lies further inside the tunnel, the pressure rise is induced by two factors: one is the nose-entry, the other is the friction effects of whole train entering into the tunnel, while the latter is almost not affected by the train nose shape. Therefore the difference for different nose shapes is relatively lower than the No. 1 point due to superposition results of these two factors. When the pressure begins to rise, the pressure rise steepens more for bulge-broad and ellipsoidal shapes than the other two shapes. However, the time for the pressure to increase from zero up to peak value is approximately the same. The peak pressure values of flat-broad and fusiform shapes are also lower than those of bulge-broad and ellipsoidal shapes. In Fig. 11(a), compared with bulge-broad shape, the peak value of the initial pressure induced by flat-broad shape is reduced by 5.3%. As mentioned earlier, the bulged-broad and ellipsoidal shapes, as well as fusiform and flat-broad shapes, these two groups both have same longitudinal nose profile lines. Therefore, this pattern of pressure difference can be attributed to

the change of longitudinal nose profile line. Furthermore, is was revealed that the horizontal nose profile line has little effect on the variation of the initial compression wave.
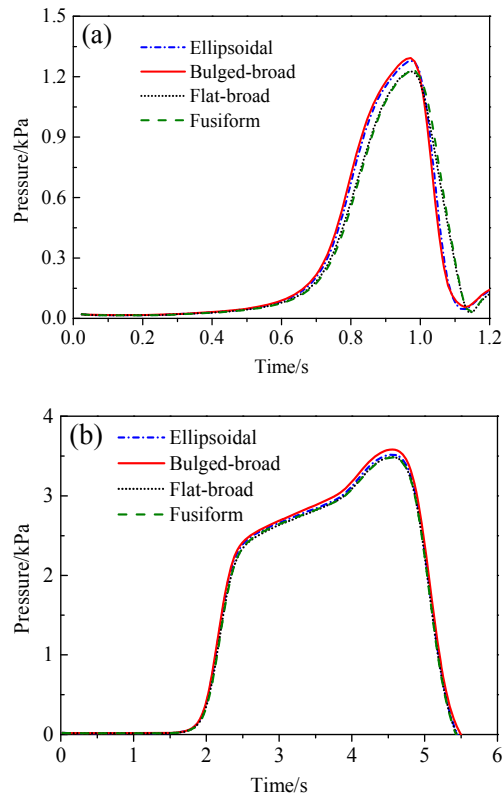

Fig. 11. Initial compression waves induced by trains of different nose shapes: (a) No. 1 measuring point; (b) No. 5 measuring point.

5.2 Pressure Transient on Train Surface

Figure 12 shows the peak-to-peak pressure of each measuring point on train surface in longitudinal direction. The measuring points of No. 1 on the nose and No. 26 on the tail are placed in the middle of the intersection side and non–intersection side (refer to Fig. 6). So Fig. 12(a) and Fig. 12(b) both contains these two points. The surface pressure on train body, whether it is intersection side or non–intersection side, the deviation of the pressure variations among the four nose shapes is relatively large only at nose and tail where the surface curvature change is quite sharp. Whereas the pressure difference on the middle cars is rather small. The pressure variations at nose and tail for trains which have the same longitudinal nose profile line are almost identical, while there is significant difference for trains which have different longitudinal nose profile lines. For instance, the pressure variations on train nose of flat-broad and fusiform shape are 5021 and 5130 Pa respectively, they both have the same longitudinal nose profile B. While the pressure variation for bugle-broad and ellipsoidal shape are 5510 and 5441 Pa respectively, they both have the same longitudinal nose profile line A. Obviously, the train surface pressure is more influenced by the longitudinal nose profile line than

horizontal nose profile line. The pressure variations on train surface of longitudinal nose profile line B are smaller than that of profile line A. Additionally, among the four different nose shapes, the highest pressure impact is on the train nose. While the pressure variation decreases along with train length direction, but rise again at tail. During the whole process of the train movement in the tunnel, the maximum pressure variation occurs on the train nose, the highest of bulge-broad shape and the lowest of flat-broad shape are 5510 Pa and 5021 Pa respectively, difference of which is 9.7%.
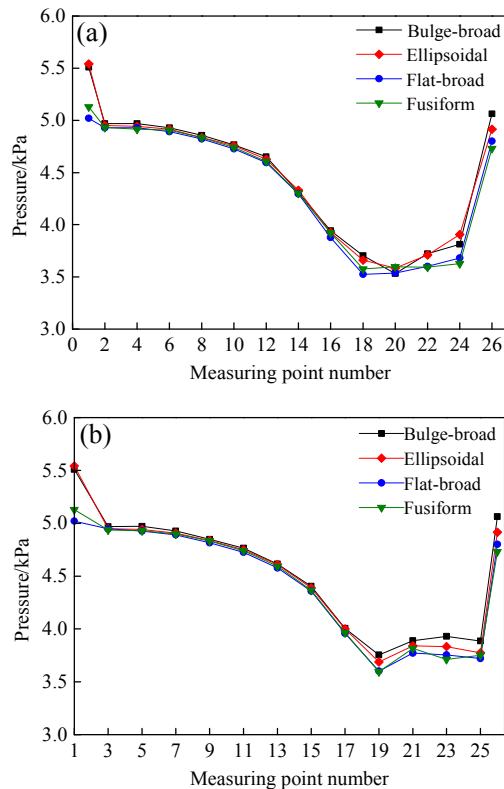

Fig. 13. Total drag of trains with different nose shapes.

Fig. 14. Time-pressure variation of No. 1 measuring point on train nose.

Fig. 12. Peak-to-peak pressure value on train surface under different nose shapes: (a) non-intersection side; (b) intersection side.

5.3 Analysis of Aerodynamic Drag

Figure 13 presents the total drag of the trains with different nose shapes passing by each other through the tunnel. EN indicates the moment when the head car enters the tunnel, NN represents the moment when two trains' nose meet each other; NT refers to the exact moment when the two trains are paralleled side by side; TT means the moment when the two trains' tail meet each other. EX stands for the moment when the head car exits the tunnel. As can be seen, the total drag variations of the trains with different nose shapes are basically the same, the pressure values are all positive, only slightly different in amplitude. Fig. 14 shows the time-pressure variation of No. 1 measuring point on train nose. The variations of the waveforms between Fig. 13 and Fig. 14 show similar trends, it is indicated that the total drag is highly correlated with the pressure variation on train nose.
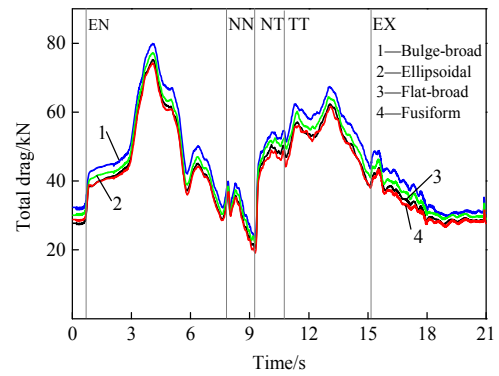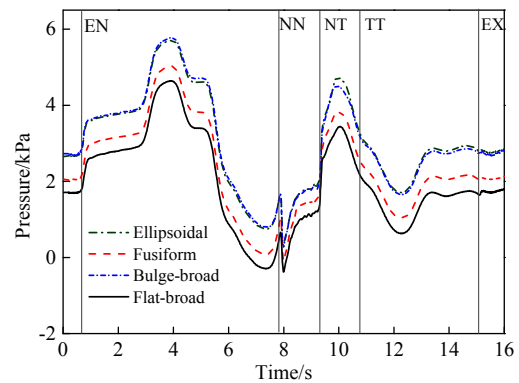
Due to the confine space of the tunnel wall, when the head car suddenly enters into the tunnel at t_{EN}=0.7 s, the air in front of the train's nose is densely compressed, producing compression waves simultaneously in both opposite directions, the total drag rises perpendicularly accordingly. When the train moves further into the tunnel from nose to tail, the compressed air releases backwards along the annular space between the train and tunnel, thus the compression effects of the air become weaker than before, and the drag increases gradually. Once the train fully enters into the tunnel, an expansion wave is formed, leading to a vacuum region at the tunnel entrance, so the drag rises dramatically and reaches the peak at t=4.2 s due to the suction force of the vacuum region. At t_{NN} =7.9 s, the drag has a pulse change due to the compressed air from both ends meet each other and rapidly release along the gap between the two trains. When the two trains passed each other after the NN moment, the drag decreases and hits the lowest value at the t_{NT}=9.3 s. Although the drag increases after the NT moment, the maximum value is still lower than that peak value before two trains meet (t=4.2 s), this is resulted from the diminution of reflected compression waves. The drag fluctuates and varies all the way through the tunnel due to the passing-by of the opposite train and successive propagations and reflections of the pressure waves. Until at t_{EX}=15.1 s, the drag firstly increases then gradually decreases and finally gets out of the influence of the tunnel pressure waves. The total drag expands from small

to large by the sequence of fusiform, flat-broad, ellipsoidal, bulge-broad shape. The maximum drag of bulge-broad shape and the minimum of fusiform shape are 79.9 kN and 74.3 kN respectively. The largest difference of the total drag attains 7.4% due to the change of nose shape. To analyse the influencing rules of the nose shapes on aerodynamic drag more intuitively, the maximum drag of trains with different nose shapes are shown in Table 2. Due to the similar aerodynamic characteristics of the middles cars, the 3rd car is chosen to represent the middle cars. As can be seen, the nose shape has largest impact on the tail car drag, smallest impact on the middle car drag, the largest drag deviation on the tail car differs 16.96%. Whether it is head car, middle car or tail car, the sequence of the drag from small to large is fusiform, followed by flat-broad, ellipsoidal, bulge-broad.

Table 2 Maximum drag of trains with different nose shapes

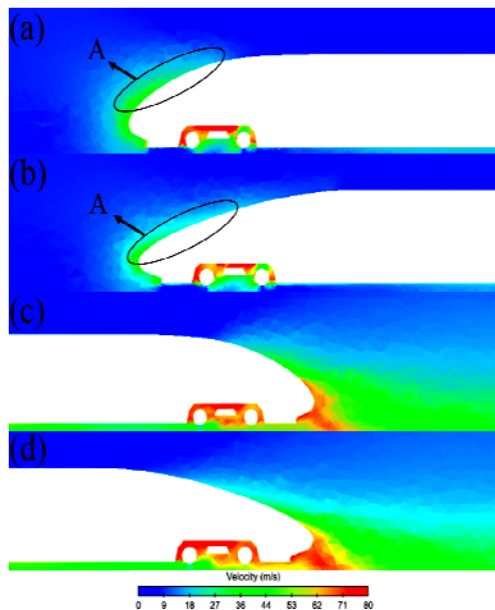| Nose shape	Head car	Middle car	Tail car
Bulge-broad	24.18	10.04	13.31
Ellipsoidal	23.91	9.86	12.86
Flat-broad	23.05	9.80	12.10
Fusiform	22.98	9.70	11.38
Deviation	5.22%	3.51%	16.96%

Fig. 15. Velocity contours around trains of different longitudinal nose profile lines: (a) head car of profile line A; (b) head car of profile line B; (c) tail car of profile line A; (d) tail car of profile line B.

By the reason that the fusiform and flat-broad shapes both have the same longitudinal nose profile line B, the profile line change of these two shapes are smoother and more fluent than the other two

shapes, so the airflow is not easily blocked and separated. Fig. 15 presents the velocity contours around trains with different longitudinal nose profile lines at t=4.5 s in the tunnel. Compared with Fig. 15(a), the distribution of the airflow velocity in Fig. 15(b) at the transition region A (i.e. from the nose to train body) is more average and gradual, so the pressure in front of the train nose is reduced accordingly. Similarly, although in Fig. 15(d) the airflow around the tail car of profile line B separates earlier than the tail car of profile line A in Fig. 15(c), but the velocity change is not that steep or abrupt. Consequently, the negative pressure at tail region is much lower and average. The pressure difference between the nose and tail is thus decreased. Hence, the pressure drag is reduced between the nose and tail. It can be concluded that the aerodynamic drag characteristics for the trains of the longitudinal nose profile line B is relatively better.

5.4 Analysis of Lateral Force.

Figure 16 presents the time-history of the head car lateral force of the four nose shapes, when the train enters into the tunnel at t=t_{EN}, the lateral force fluctuates with a sudden change of air pressure in the tunnel. When the train is entirely running inside the tunnel between the EN and the NN moment, as well as the NT and the EX moment followed, the lateral force appears to be slightly negative and remain almost constant. This is mainly because the flow field inside the double-track tunnel is unsymmetrical and the negative pressure on the train surface closer to the tunnel wall side (non-intersection side) is greater, hence, a negative lateral force appears to slightly push the train towards the tunnel wall. When the two trains meet each other at t=t_{NN}, the high pressure region around the train noses push the head cars laterally away from each other. As a result, the lateral force has a pulse change, first negative and then positive. Between the moment of the NN and the NT, due to passing by the opposite train's windshields, the compressed air between the two trains' gap successively releases towards the windshield intervals for several times. Consequently, the lateral force has several obvious fluctuations. Once the opposite train's tail passes by at t=t_{NT}, the lateral force has another pulse change similar to that of the NN moment. When the head car leaves the tunnel at t=t_{EX}, the boundary condition suddenly changed into the open field from the confined airspace inside the tunnel, an expansion wave is generated and spreads along the tunnel and causes the pressure drop. As mentioned in Section 3.2, the train is running on the left side of the track, the non-intersection side is much narrower, so the flow field is not symmetrical, the pressure on the train body closer the tunnel wall decreases more, therefore, the fluctuations of the lateral force are observed at t=t_{EX}. When the train completely leaves the tunnel, the lateral force is not influenced by the tunnel anymore and regain to zero. From the perspective of peak-to-peak value of the lateral force, the lateral force at the NN moment is higher than that of the NT moment, additionally, the lateral force is more

influenced at the EX moment than that of the EN moment.

In order to analyse the difference of lateral force of the trains under different nose shapes, the peak-to-peak lateral force of each car of these four shapes are presented in Fig. 17. As can be seen, the lateral force acting on the head car and tail car is quite higher, while the six middle cars are relatively lower. Moreover, it can be deduced that the lateral force characteristics is more influenced by longitudinal nose profile line. For on the same conditions, lateral force of trains with the longitudinal nose profile line B (i.e. fusiform, flat broad shape) are relatively lower. The influencing rules on lateral force of the head car, tail car and six middle cars are identical. The sequence from small to large is flat-broad, fusiform, bulge-broad, ellipsoidal shape. The nose shape has significant difference of lateral force on the tail car, the maximum deviation attains 31.5%.
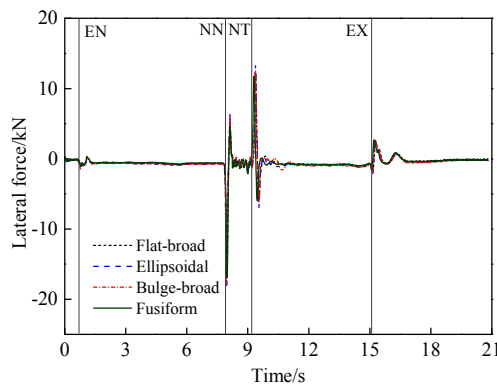

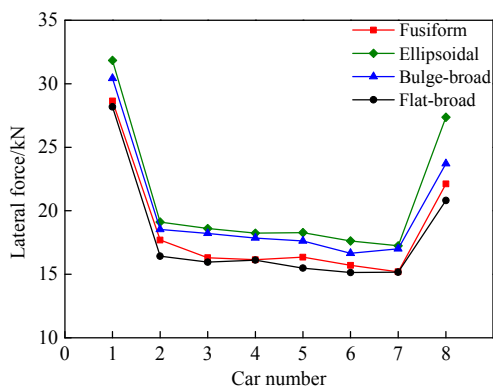**Fig. 16. Time-history of lateral force of the head car under the four nose shapes.**

Fig. 17. Peak-to-peak lateral force of the each car of trains with different nose shapes.

6. CONCLUSIONS

The turbulent flow around the trains of different nose shapes passing by each other through a tunnel were computed using three dimensional, compressible, RNG *k*– turbulence model to uncover the aerodynamic performance. The numerical model was validated by comparing with the field measurement results. Then, the model was used to examine the transient pressure and aerodynamic loadings caused by opposing trains of different nose shapes passing by each other through a tunnel. The results of the study are summarized as follows:

1) In the whole process of the two opposing trains passing by each other in a tunnel at 250 km/h, the nose shape has less influence on the tunnel wall pressure at the same location from the tunnel entry, the maximum deviation is 4.7%; surface pressure on the head and tail car is more influenced by the nose shape while middle cars are less influenced, the maximum deviation of pressure variation on trains among different nose shapes occurs on the train nose, the difference is about 9.7%.

2) The aerodynamic drag is decreased by the sequence of bulge-broad, ellipsoidal, flat-broad, fusiform shape. Compared with bulge-broad shape, the total drag of fusiform shape is reduced by 7.4%. Lateral force gradually decreases by the sequence of ellipsoidal, followed by bulge-broad, fusiform, flat-broad shape, the maximum deviation on the tail car attains 31.5% due to the change of nose shape.

3) Aerodynamic performance of two opposing trains passing by each other in a tunnel is little influenced by the horizontal nose profile line, but is more influenced by the longitudinal nose profile line. The aerodynamic performance for trains with the longitudinal nose profile line B (i.e. fusiform, flat-broad shape) is relatively better when passing by each other through a tunnel.

REFERENCES

Choi J. K. and K. H. Kim (2014). Effects of nose shape and tunnel cross-sectional area on aerodynamic drag of train traveling in tunnels. *Tunnelling & Underground Space Technology*, 41, 62-73.

Chu, C. R., S. Y. Chien, C. Y. Wang and T. R. Wu (2014). Numerical simulation of two trains intersecting in a tunnel. *Tunnelling & Underground Space Technology* 42(5), 161-174.

Fujii, K. and T. Ogawa (1995). Aerodynamics of high speed trains passing by each other. *Computers and Fluids* 24(8), 897-908.

Gilbert, T., C. J. Baker and A. Quinn (2013). Gusts caused by high-speed trains in confined spaces

and tunnels. *Journal of Wind Engineering and Industrial Aerodynamics* 121(5), 39-48.

Hwang, J. and D. H. Lee (2013). Numerical simulation of flow field around high speed trains passing by each other. *Fluids & Thermal Engineering* 44(3), 451-464.

Ikeda, M., K. Yoshida and M. Suzuki (2003). Optimization of panhead shape for high-speed train using CFD. *Jointed railway technology symposium*. The Japan Society of Mechanical Engineers.

Kikuchi, K., M. Iida and T. Fukuda (2011). Optimization of train nose shape for reducing micro-pressure wave radiated from tunnel exit. *Journal of low frequency noise vibration and active Control* 30(1),1-19.

Ko, Y. Y., C. H. Chen, I. T. Hoe and S. T. Wang (2012). Field measurements of aerodynamic pressures in tunnels induced by high speed trains. *Journal of Wind Engineering and Industrial Aerodynamics* 100(1), 19-29.

Ku, Y. C., J. H. Rho and S. H. Yun (2010). Optimal cross-sectional area distribution of a high-speed train nose to minimize the tunnel micro-pressure wave. *Structural & Multidisciplinary Optimization* 42(6), 965-976.

Kwon, H. B., T. Y. Kim, D. H. Lee and M. S. Kim (2003). Numerical simulation of unsteady compressible flows induced by a high-speed train passing through a tunnel. *Proceedings of the Institution of Mechanical Engineers Part F Journal of Rail and Rapid Transit* 217(2),111-124.

Lee, J. and J. Kim (2007). Approximate optimization of high-speed train nose shape for reducing micro pressure wave. *Structural and Multidisciplinary Optimization* 35(1),79-87.

Li, R., W. Zhang, Z. Ning, B. Liu, D. Zou and W. Liu (2016). Influence of a high-speed train passing through a tunnel on pantograph aerodynamics and pantograph-catenary interaction. *Proceedings of the Institution of Mechanical Engineers Part F Journal of Rail and Rapid Transit* 231(2), 198-210.

Niu, J., D. Zhou, X. Liang, T. Liu and S. Liu (2017). Numerical study on the aerodynamic pressure of a metro train running between two adjacent platforms. *Tunnelling & Underground Space Technology* 65, 187-199.

Ozawa, S. and T. Maeda (1988). Tunnel entrance hoods for reduction of micro-pressure wave. *Railway Technical Research Institute Quarterly Reports*, 29.

Riccoa, P., A. Baronb and P. Moltenib (2007). Nature of pressure waves induced by a high-speed train travelling through a tunnel. *Journal of Wind Engineering and Industrial Aerodynamics* 95(8), 781-808.

Wittkowski, M. (2015). Passenger comfort on high-speed trains: effect of tunnel noise on the subjective assessment of pressure variations. *Ergonomics* 58(6),1022-1031.

Xiang, X. T. and L. P. Xue (2010). Tunnel hood effects on high speed train-tunnel compression wave. *Journal of Hydrodynamics* 22(5), 940-947.

Yang, W. C., C. He and L. M. Peng (2013). The calculation of train slipstreams on platform of underground high-speed rail station. *Advanced Materials Research* 842, 445-448.

Zhang, M. L., Y. R. Yang and L. Lu (2011). Numerical Simulation of Two High Speed Trains Passing by each other in a Long Tunnel. *Applied Mechanics and Materials*, 117-119(11), 670-673.